Wu, S., Yu, Y., Yang, T., Xue, M., Tilmann, F., Chen, H. (2022): Crustal Structure of the Indochina Peninsula From Ambient Noise Tomography. - Journal of Geophysical Research: Solid Earth, 127, 5, e2021JB023384.

https://doi.org/10.1029/2021JB023384

JGR Solid Earth

RESEARCH ARTICLE
10.1029/2021JB023384

Crustal Structure of the Indochina Peninsula From Ambient Noise Tomography

Shanshan Wu[1,2], Youqiang Yu[3,4], Ting Yang[2,5], Mei Xue[3], Frederik Tilmann[4,6], and Haopeng Chen[7]

[1]Shanghai Earthquake Administration, Shanghai, China, [2]Shanghai Sheshan National Geophysical Observatory, Shanghai, China, [3]State Key Laboratory of Marine Geology, Tongji University, Shanghai, China, [4]GFZ German Research Centre for Geosciences, Potsdam, Germany, [5]Department of Ocean Science and Engineering, Southern University of Science and Technology, Shenzhen, China, [6]Institute for Geological Sciences, Freie Universität Berlin, Berlin, Germany, [7]Department of Surveying Engineering, School of Civil and Transportation, Guangdong University of Technology, Guangzhou, China

Key Points:

- A 3-D crustal shear-wave velocity (Vs) model was constructed for the Indochina Peninsula from ambient noise tomography
- Low-Vs in the middle-lower crust of the Shan-Thai Block may represent the southern extension of the crustal flow from SE Tibet
- The crust of the rigid Khorat Plateau has been partially modified by intrusion of mantle-derived melts

Supporting Information:

Supporting Information may be found in the online version of this article.

Correspondence to:

Y. Yu,
yuyouqiang@tongji.edu.cn

Citation:

Wu, S., Yu, Y., Yang, T., Xue, M., Tilmann, F., & Chen, H. (2022). Crustal structure of the Indochina Peninsula from ambient noise tomography. *Journal of Geophysical Research: Solid Earth*, *127*, e2021JB023384. https://doi.org/10.1029/2021JB023384

Received 9 OCT 2021
Accepted 26 APR 2022

Abstract The collision between the Indian and Eurasian plates promotes the southeastward extrusion of the Indochina Peninsula while the internal dynamics of its crustal deformation remain enigmatic. Here, we make use of seismic data from 38 stations and employ the ambient noise tomography to construct a 3-D crustal shear-wave velocity (Vs) model beneath the Indochina Peninsula. A low-Vs anomaly is revealed in the mid-lower crust of the Shan-Thai Block and probably corresponds to the southern extension of the crustal flow from SE Tibet. Although the Khorat Plateau behaves as a rigid block, the observed low-Vs anomalies in the lower crust and also below the Moho indicate that the crust may have been partially modified by mantle-derived melts. The strike-slip shearing motions of the Red River Fault may have dominantly developed crustal deformation at its western flank where a low-Vs anomaly is observed at the upper-middle crust.

Plain Language Summary The Indochina Peninsula was believed to behave as a rigid block where significant southeastward extrusion and clockwise rotation have occurred in response to the collision between the Indian and Eurasian plates. Here, we employ ambient noise data to obtain the shear-wave velocity (Vs) images and find deformations in the interior of the crust beneath the Indochina Peninsula. A low-Vs anomaly is observed in the mid-lower crust of the Shan-Thai Block and represents the crustal flow from SE Tibet. The crust of the Khorat Plateau, the core of the Indochina Block, has been partially modified by mantle-derived melts. The strike-slip shearing motions of the Red River Fault have brought crustal deformation at its southwestern flank characterized as a low-Vs anomaly in the upper-middle crust.

1. Introduction

Since the Cenozoic (~50 Ma), the collision between the Indian and Eurasian plates not only led to the formation of the Himalayan–Tibetan orogen, but also played a significant role in controlling the tectonics of SE Asia (Huchon et al., 1994; Tapponnier et al., 1982). The Indochina Peninsula (IP), situated adjacent to the SE Tibetan Plateau, mainly composes of the Shan-Thai (also referred to Sibumasu) and Indochina Blocks (e.g., Leloup et al., 2001; Morley, 2002), which are bounded by the South China Block to the east and the Indo-Burma microplate to the west (Figure 1). The continuous northward indentation of the Indian plate into the Eurasian plate is believed to have caused about 700 km southeastward extrusion of the IP along a series of bounding strike-slip faults such as the Red River Fault (RRF) and Wang-Chao Fault (WCF; e.g., Huchon et al., 1994; Leloup et al., 1995; Tapponnier et al., 1982). The extrusion of the IP was further proposed to have, among other processes, initiated the opening of the South China Sea (e.g., Tapponnier et al., 1982). Formation of the IP, which compromises several Gondwana fragments (Charusiri et al., 2002), can be dated back to the Late Triassic when the Shan-Thai Block collided with the Indochina Block along the place of the Dien Bien Phu Fault (DBPF), as evidenced by outcrops of oceanic subduction-related volcanic granitoid rocks (Charusiri et al., 1993; Lepvrier et al., 2004; Racey, 2009). Since the Cenozoic, the IP appears to have behaved as a rigid block, which has also underwent clockwise rotation (e.g., Achache et al., 1983; Sato et al., 2007; Tapponnier et al., 1982, 1986). However, whether the crust of the IP experiences significant deformations in response to tectonic events such as the southeastward extrusion and clockwise rotation remains unclear.

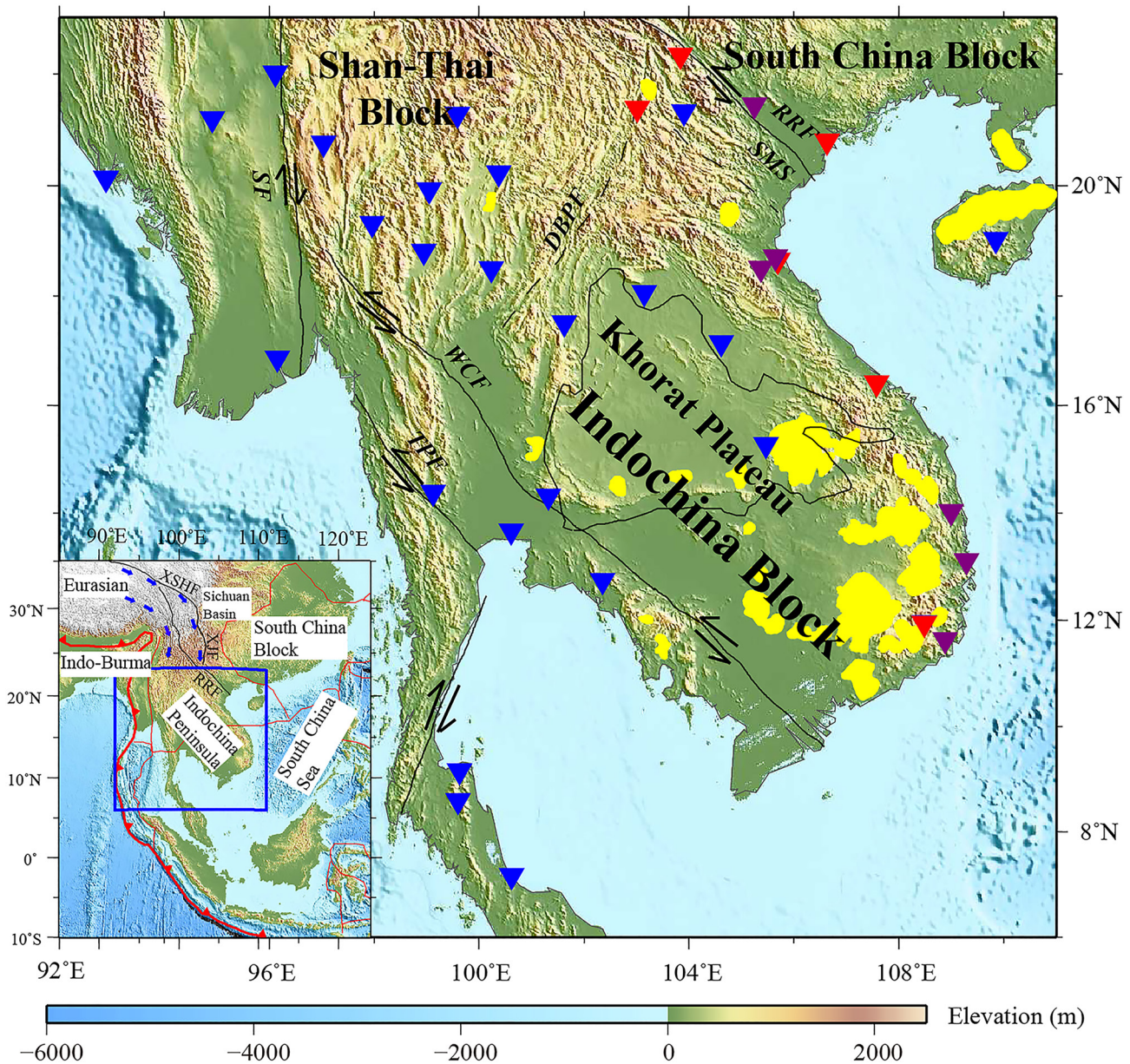

Figure 1. Topographic map of the Indochina Peninsula displaying the major tectonic provinces and station distributions (triangles). Blue, purple, and red triangles represent stations from IRIS, Tongji University, and the University of Tokyo, respectively. Black solid and dashed lines correspond to major faults and sutures (Leloup et al., 1995; Takemoto et al., 2009). DBPF, Dien Bien Phu Fault; RRF, Red River Fault; SF, Sagaing Fault; SMS, Song Ma Suture; TPF, Three Pagodas Fault; WCF, Wang-Chao Fault; XJF, Xiaojiang Fault; XSHF, Xianshuihe Fault. The black rectangle in the inset map shows the location of the study area. The thick and thin red lines represent the trenches and plate boundaries (Bird, 2003), respectively. The blue arrows depict the southeast to south-directed lower-crustal flow channels south of the Sichuan block, modified from D. Bai et al., 2010). The yellow shaded areas are the Cenozoic volcanic centers (Fedorov & Koloskov, 2005; Hoang & Flower, 1998).

The Khorat Plateau (the core of the Indochina Block) is imaged to have a typical continental crustal thickness of 36.9 ± 3 km and Vp/Vs ratio of 1.74 ± 0.04 (Yu, Hung, et al., 2017) and a lithospheric thickness of about 200 km (Chen et al., 2021; T. Yang et al., 2015), suggesting that the interior of the IP may have retained continental keel thus having been shielded from significant internal deformation and reworking (e.g., Takemoto et al., 2009). However, crustal material from the Tibet Plateau has been proposed to escape outward by a middle-lower-crustal channel flow (Clark & Royden, 2000; Royden et al., 2008). One branch of the lower-crustal flow is deflected by the rigid Sichuan basin and flows southward into the IP (Figure 1), which may cause internal deformations in the crust of the IP (Bao, Sun, et al., 2015; Royden et al., 2008; L. Zhao et al., 2013). An intra-lower-crustal low-velocity zone (LVZ) was revealed in northern Vietnam (L. Bai et al., 2010) and terminated to the west at the DBPF.

The eastern branch of the LVZs in the SE Tibet exhibits strong attenuation and high-electrical conductivity (D. Bai et al., 2010; L. Zhao et al., 2013) and is revealed to extend southward into the IP (Bao, Sun, et al., 2015) based on joint inversion of Rayleigh-wave dispersion and receiver functions (RFs). Ambient noise tomography in the area adjacent to SE Tibet also imaged a middle-lower-crustal LVZ at the Xiaojiang Fault Zone, which crossed over the RRF into Vietnam (Qiao et al., 2018). However, the southern boundary of the lower-crustal flow and whether the interior of the IP is affected by the aforementioned flow system remain unresolved due to the lack of a detailed 3-D image on its crustal structure.

Whereas a large-scale 3-D shear-wave velocity (Vs) model was obtained for the South China Sea and its adjacent areas including part of the IP from Rayleigh-wave analysis of ambient noise and earthquake data (Chen et al., 2021; J. Zhao et al., 2019) while the whole IP area is not well imaged. Here, we make use of all available seismic broadband data to obtain a 3-D image of crustal Vs structure beneath the IP by conducting ambient noise tomography. Our observations indicate that the lower-crustal flow from the SE Tibet has propagated southward into the Shan-Thai Block and terminated at the DBPF. The core of the Indochina Block, the Khorat Plateau, has been partially modified by the intrusion of mantle-derived melts. Finally, the strike-slip shearing of the RRF has brought significant crustal deformations at its western flank.

2. Ambient Noise Data and Tomographic Inversion

2.1. Ambient Noise Data

All waveform data were collected from three sources with a total of 38 stations among which 6 portable stations were deployed by Tongji University in Vietnam from 2009 to 2012 (T. Yang et al., 2015), data from 26 stations were requested from the Incorporated Research Institutions for Seismology (IRIS) Data Management Center belonging to five networks (IC, IU, MM, RM, and TM), and another 6 stations were operated by the University of Tokyo during 2000–2005 (L. Bai et al., 2010). We have applied similar procedures to process raw seismic data of the vertical components as those applied by Bensen et al. (2007) and Y. Yang et al. (2007) for the ambient noise tomography. All raw seismic data were first cut to 1-day segments and resampled to 1 Hz with the removal of instrument responses, which were then band-pass filtered within the period band of 5–100 s. The time domain normalization and spectral whitening were also performed to remove possible effects of earthquakes and other irregularities with the purpose of broadening the bandwidth of ambient noise data (Y. Yang et al., 2007).

Cross correlations of daily data from each station pair were computed and then stacked together to enhance the signal-to-noise ratio (SNR; Bensen et al., 2007). An example of cross correlations between station QIZ and the other synchronous stations (Figure S1a in Supporting Information S1) displays clear surface wave signals at both positive and negative lag times with a symmetric shape. To further enhance the SNR of the stacked cross correlations, the positive and negative signals for each cross-correlation are averaged and stacked to generate the symmetric waveforms (Bensen et al., 2007). We then employed the automatic frequency–time analysis (AFTAN) method to extract Rayleigh-wave phase velocity dispersion curves at each station pair with two steps (Levshin & Ritzwoller, 2001). The waveforms were first narrow-phase filtered with a series of central frequency to create the energy amplitude spectrum changing with arrival time and frequency. The arrival time of maximum amplitude spectrum was then automatically tracked and used to calculate the group velocity, with phase velocity estimated by considering the phase at the group arrival time (Figure S2 in Supporting Information S1), which were finally recalculated after applying the phase-matched filtered AFTAN (Bensen et al., 2007). All the automatically picked dispersion curves were visually examined in the context of the spectrograms and by comparing with those calculated from the AK135 Earth model (Kennett et al., 1995). They were selected by considering a continuously traced curve of maximum amplitude energy in the amplitude spectrum without significant heterogeneities such as irregular shapes or obvious outliers (Figures S1b and S2 in Supporting Information S1).

Two other parameters were also employed to keep stability and accuracy of the inversion during the automatically selection procedure (Yao et al., 2006). First, the interstation distance of dispersion measurement at each period is set to have a minimum value of two wavelengths (Fan & Chen, 2019; X. Yang et al., 2021). Second, the phase velocities measured from cross correlations with a SNR less than 10 were dropped. The SNR is calculated by the ratio between the maximum amplitude within the signal window (theoretical arrival times of Rayleigh wave at 5 and 100 s) and the root-mean-square of noise within the window trailing the end of signal by 500 s (Bensen

et al., 2007). Most of the study area is covered by a reasonable number of raypaths for periods 8–30 s after quality control (Figures S3 and S4 in Supporting Information S1).

2.2. Phase Velocity Tomography

Rayleigh-wave phase velocity variations were obtained by adopting a linear inversion method (Tarantola & Valette, 1982) for each period. The model is parametrized in terms of slowness perturbations. The a priori model covariance function is expressed as Equation 1 and represents the covariance between two points at x and x' (Chen et al., 2014; Montagner & Nataf, 1986; Yao et al., 2006):

$$C_{m_0}\left(x, x'\right) = \sigma_{m_0}^2 \exp\left[-\frac{(x-x')^2}{2L^2}\right] \tag{1}$$

and

$$\sigma_{m_0} = \sigma_{c_0}/c_0^2 \tag{2}$$

where L is the correlation length, σ_{c_0} is the a priori phase velocity variance, c_0 is the average phase velocity value at each period, and σ_{m_0} is the prior model (slowness) error. L controls smoothness of the phase velocity variations with a spatial resolution of about $2L$ and is mainly determined by considering the wavelength and raypath density at each period (Chen et al., 2014; Yao et al., 2006). Here, we considered that the surface wave tomography is based on high-frequency asymptotic ray theory and requires that the scale of the inverted anomaly body should be larger than the wavelength at corresponding period, implying a minimal value of ~100 km, the approximate wavelength at 30 s (Yao et al., 2005). In addition, we conducted a series of checkboard resolution tests with different values of the correlation length, and finally set L to 165 km as the best compromise between resolution and stability in our linear inversion. σ_{c_0} is assigned as 1% of the average phase velocity value at each period (Chen et al., 2014; Yao et al., 2006). A predicted phase travel time is calculated based on the great-circle path and the region is gridded by $0.5° \times 0.5°$.

The linear inversion for phase velocity tomography is actually conducted by following a two-step procedure (Chen et al., 2014). We first determined a preliminary inversion by setting the *a priori* travel time misfits and thus the weights of all raypaths to be the same. In the second step, posterior travel time misfits of the first inversion were used as the priori travel time misfits in the second step; raypaths with larger posteriori travel time misfits thus had smaller weight. Phase velocities of 8–30 s were adopted in the inversion by considering the distributions of raypath density (Figure 2b) as the average SNR of phase velocities at longer periods will drop rapidly (Lin et al., 2008). The depth sensitivity kernel curves of average Rayleigh-wave phase velocities at different periods with respect to S wave velocity (Figure S6 in Supporting Information S1) show that most of the crustal and uppermost mantle structures can be resolved based on data from the period band of 8–30 s.

2.3. Phase Velocity Maps and Resolution Tests

The averaged 1-D phase velocities (Figure 2) at short period (<22 s) predicted from the first inversion are very close to the IASP91 Earth model (Kennett & Engdahl, 1991), which represents typical continental structure. 2-D phase velocity anomaly map at each period was computed relative to the average 1-D phase velocity model and displays close relationship with regional tectonic features (Figure 3). A localized low-velocity anomaly at a period of 10 s is observed in the center of the Khorat Plateau where thick sediments exist (Figure 3a). At 20 s, the whole Khorat Plateau is characterized by low-velocity anomalies. The Shan-Thai Block and the Khorat Plateau have high-velocity anomalies at the period of 26 s with low-velocity anomaly near the southern terminus of the DBPF in between. The Sagaing Fault appears to separate lower velocities in the west from faster velocities in the east at lower periods, though velocity distribution in this fault boundary area is affected by smearing at the longer periods.

Checkerboard tests were performed in order to evaluate the resolution of the phase velocity maps at periods of 10, 12, 16, 20, and 26 s. The checkerboard grid interval is set as 3°. Positive and negative velocity anomalies with an absolute value of 5% were alternatively assigned to the 3-D grid nodes. We calculated average phase dispersion curves for the actual ray distribution at each period and then inverted them with the same parameters in actual

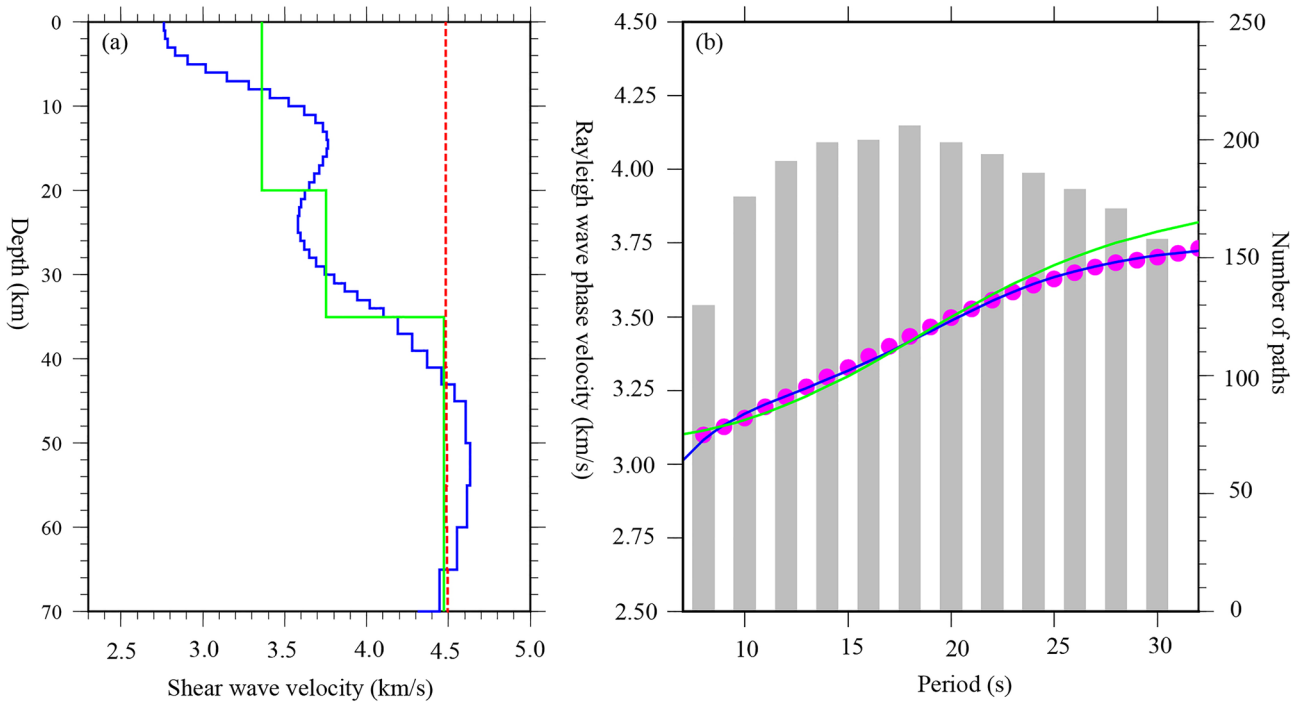

Figure 2. Analysis of the starting 1-D shear-wave velocity (Vs) model and the correspondingly theoretical Rayleigh-wave dispersion curves. (a) Starting model for the Rayleigh-wave phase velocity inversions. The red dashed line is the initial Vs model for 1-D average Rayleigh-wave phase velocity inversion of the observations (magenta dots) in (b) and the subsequent resulting 1-D Vs model is displayed in blue line. The green line represents the IASP91 Earth model. (b) Theoretical dispersion curves computed from the corresponding (color) Vs models. The gray bars represent the number of paths for each period of Rayleigh-wave phase velocity inversion.

inversion. The checkerboard test results indicate that the input model is recovered for most of the study area at all periods (Figure 4). Some smearing artifacts at the margins of the model domain are visible at longer periods (>20 s), particularly in the westernmost area.

3. Shear-Wave Velocity Inversion

We employed the iterative least squares inversion algorithm (Herrmann, 2013) to invert for the 1-D Vs model at each grid point. The initial model for the inversion is based on the averaged 1-D phase velocity dispersion. At the end, all resulting 1-D Vs models are assembled to construct the 3-D Vs model. The phase velocity maps were sampled with a horizontal grid space of 0.5°. For the depth inversion, 48 layers are used with a maximum depth of 80 km. The depth interval changes from 1 km in the upper 35 layers to 2–5 km for the lower layers by considering the increasing width of sensitivity kernel with longer period.

The variations of the Moho depths in the starting model have been considered by combing results from CRUST1.0 model (Laske et al., 2013) and previous RF studies (Nguyen et al., 2013; Noisagool et al., 2014; Yu, Hung, et al., 2017) to constrain the Vs depth inversion. Velocity changes are allowed at the two layers adjacent to the Moho depths determined from previous studies (Herrmann, 2013). The corresponding Vp structures were determined by assuming the spatially variable Vp/Vs ratios from RF investigations (Nguyen et al., 2013; Noisagool et al., 2014; Yu, Hung, et al., 2017) and then employed to compute the corresponding density structures through an empirical formula (Brocher, 2005). A total of 60 iterations have been applied for the inversion. The damping factor is set as 0.5 for the first 10 iterations and then changed to 0.1 for the remaining 50 iterations in order to increase the stability of the inversion.

The effects of initial models and data uncertainties on our inversion results have been examined at two representative grid points (96.5°E, 20.5°N) and (104.5°E, 17.0°N). We have designed three alternative initial models. Two of them have Vs increased or decreased by 5% with respect to the standard initial model, respectively (Figure 5). Constant velocities were assigned for the crust and upper mantle (Figures 5a and 5c), separated by a 10 km gradient zone, to generate the third initial model. All the resulting theoretical dispersion curves predicted from

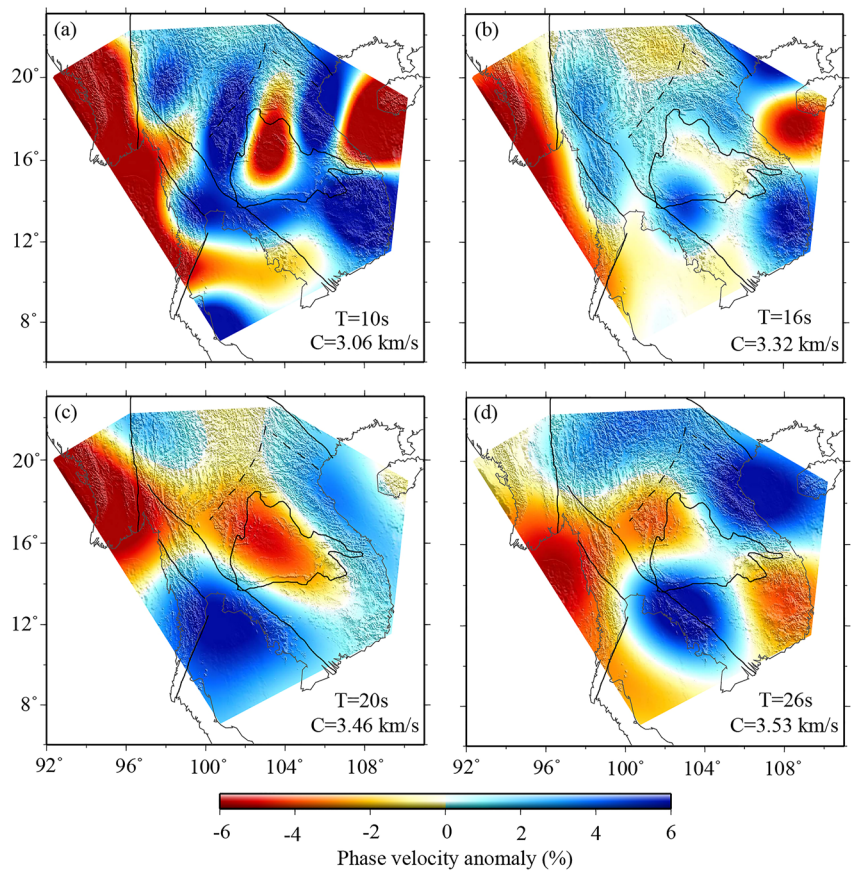

Figure 3. Maps of Rayleigh-wave phase velocity anomalies from ambient noise tomography at 10 s (a), 16 s (b), 20 s (c), and 26 s (d) period. The background reference Rayleigh-wave phase velocity (based on regional average, see Figure 2) is labeled at the bottom right.

these different initial models are almost the same and fit quite well with the observations, which indicates that the starting models have little effect on the inversion results, consistent with previous results (Cheng et al., 2013; Wei et al., 2020). We have generated 100 sets of dispersion data with ±1% random deviations from the observed one (Cheng et al., 2013; Wei et al., 2020) and employed the same procedures used for the final inversion to invert for the 1-D Vs models. The resulting 1-D Vs structures from the 100 inversions at the two points show quite similar trend of velocity variations in both the crust and mantle with the actual results (Figure 6). The main features of the resulting Vs anomalies were further evaluated by conducting synthetic tests with the input models designed by referring to the actual inversion results (Figure S7 in Supporting Information S1).

4. Results

The resulting Vs anomalies are shown as map views (Figure 7) and in cross section (Figure 8). Low-velocity anomalies are revealed in the shallow crust at the center of the Khorat Plateau and the coastal areas (Figure 7a) where extensive sediments exist. Geological studies indicate that the Khorat Plateau has accumulated 5 km thick Mesozoic strata (Takemoto et al., 2009). The upper crust (Figure 7b) of both the Shan-Thai Block and the Khorat Plateau is imaged to have high-velocity anomalies, which are surrounded by low-velocity anomalies near the WCF and RRF. A low-velocity anomaly southwest of the RRF extends to a depth of about 20 km (Figure 8, LV3) but is not aligned with it. Another distinct low-velocity anomaly is revealed in the middle-lower crust of the Shan-Thai Block and terminates at the DBPF (Figure 8, LV1). In addition, we also observe a low-velocity anomaly in the lower crust of the Khorat Plateau (Figure 8, LV2), which is not connected to those below the Shan-Thai Block and situates in a much larger depth (Figures 7 and 8c).

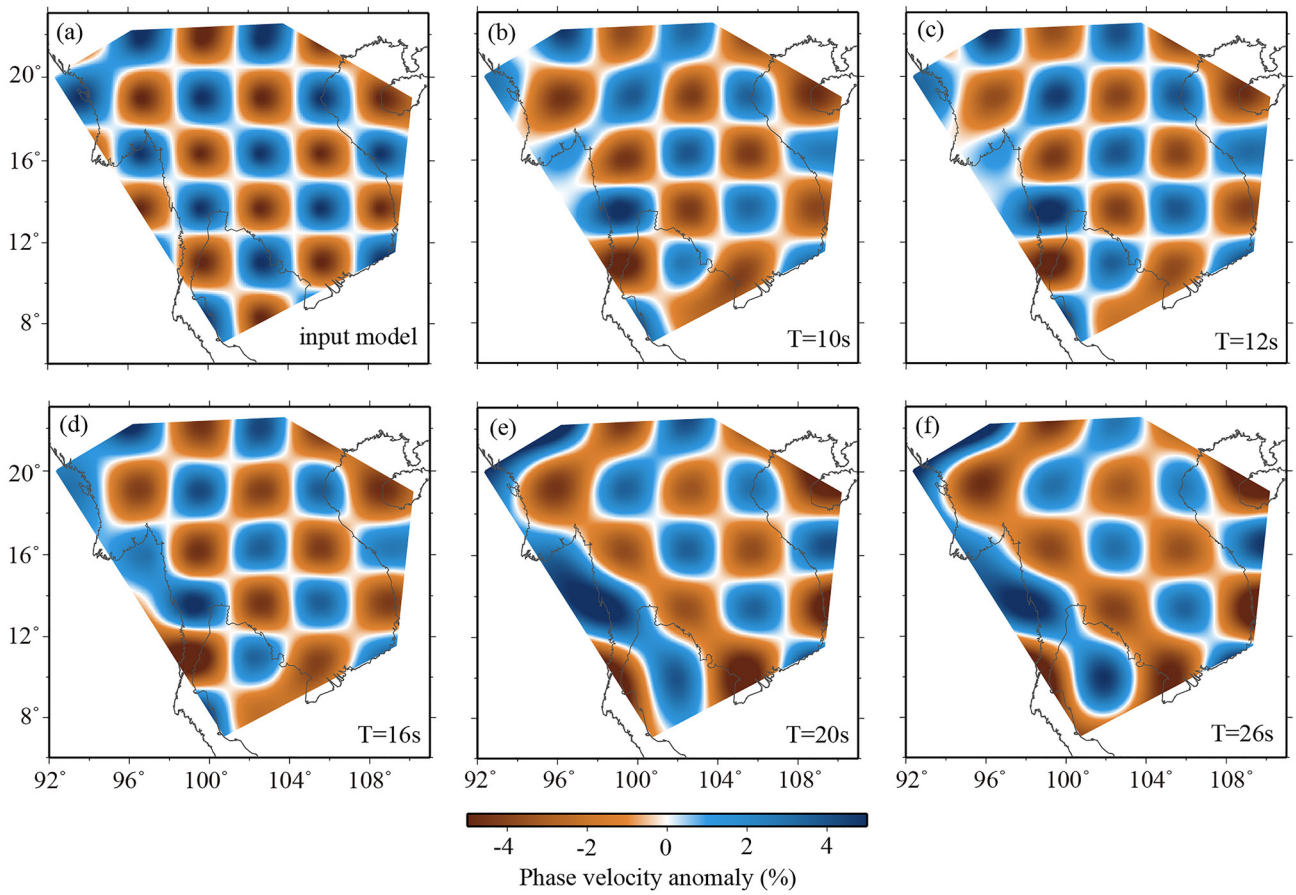

Figure 4. Checkerboard resolution tests for ambient noise tomography. The input model consists of 3° × 3° checker is shown in (a) with the inverted results at periods of 10 s (b), 12 s (c), 16 s (d), 20 s (e), and 26 s (f).

The 3-D Vs model also provides information on the lateral variations of crustal thickness. The Moho depths integrated from the CRUST1.0 model (Laske et al., 2013) and a series of RF studies (Nguyen et al., 2013; Noisagool et al., 2014; Yu, Hung, et al., 2017) are roughly coincident with the 4.0 km/s Vs contour in our model (Figure 8). The Khorat Plateau is revealed to possess a thicker crust relative to the Shan-Thai Block. The average Moho depth of the Shan-Thai Block is determined to be 31 km and that of the Khorat Plateau varies from 37 to 39 km according to observations from RF investigations (Noisagool et al., 2014; Yu, Hung, et al., 2017). If we consider Vs reaching 4.0 km/s as the Moho depth (Bao, Song, et al., 2015), we can see that the average crustal thickness of the Shan-Thai Block is roughly ∼33 km and that of the Khorat Plateau is much deeper of roughly ∼40 km (Figure 8).

5. Discussion

5.1. Middle-Lower-Crustal Flow Beneath the Shan-Thai Block

LVZs in the middle-lower crust of SE Tibet (Figure 9) have been interpreted as ductile channel flows for transportation of mechanically weak materials from the interior of Tibet (e.g., Bao, Sun, et al., 2015; Sun et al., 2014). These LVZs are also characterized as possessing high-electrical conductivity (D. Bai et al., 2010), low-Q value (L. Zhao et al., 2013), high heat flow (Hu et al., 2000), strong positive radial anisotropy (H. Huang et al., 2010), and systematic north-south crustal azimuthal anisotropy (e.g., Kong et al., 2016; C. Liu et al., 2019). In map view, the LVZs form two channels (Figure 9) which are aligned with the major strike-slip faults (e.g., Bao, Sun, et al., 2015). The widely distributed LVZ beneath the Shan-Thai Block observed by us at depths of 15–25 km (LV1 in Figures 7 and 8) may represent the southern extension of the eastern branch of this crustal ductile flow from SE Tibet. The RF analysis of L. Bai et al. (2010) also revealed an intra-lower-crustal LVZ at isolated stations in the Shan-Thai Block. The eastern branch of the crustal flow has been proposed to flow across the

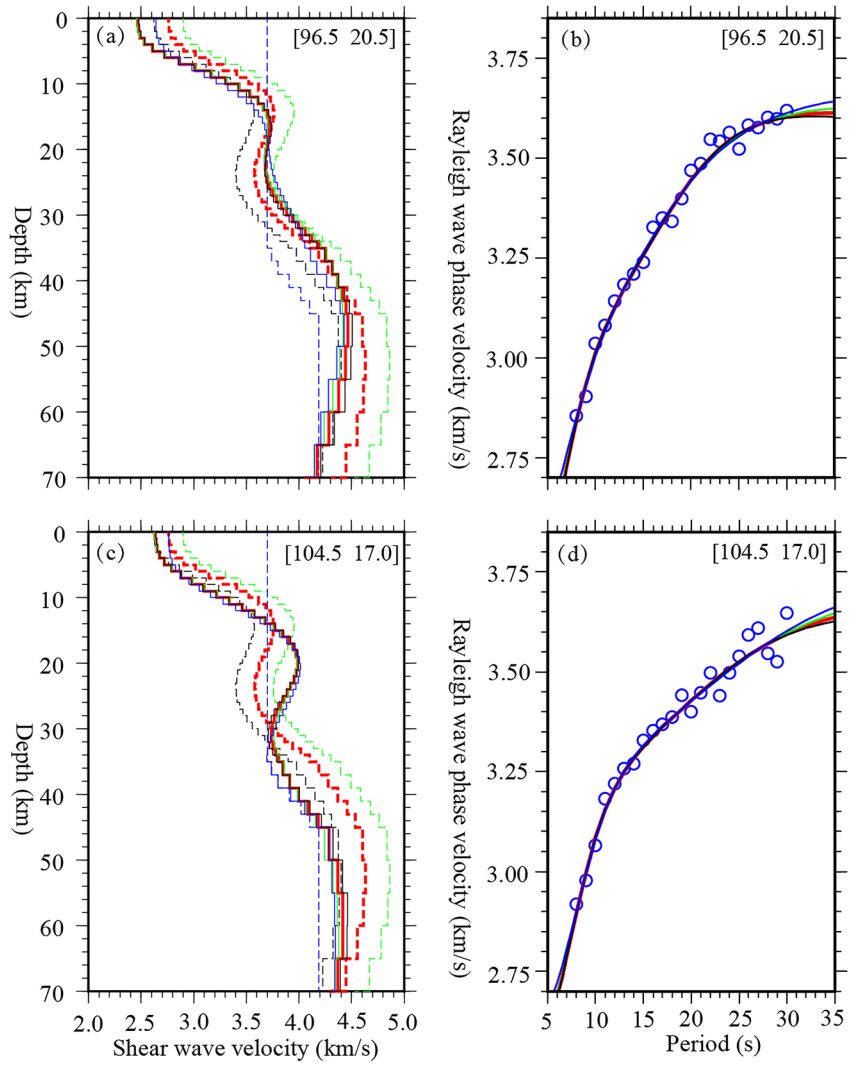

Figure 5. Dependency test of initial models on Vs inversion from two typical locations in the study region. The coordinates of these two points are shown in the top right. (a, c) Display the initial (dashed lines) and inverted (solid lines) 1-D Vs models. Green and black dashed lines were designed as +5% and −5% deviations from the optimal initial model (red dashed line), respectively. The blue dashed line was assigned with constant Vs values in the crust and mantle, separated by a gradient zone. (b, d) The theoretical Rayleigh-wave dispersion curves based on the corresponding initial models in (a) and (c), respectively. Blue circles represent the real observations.

RRF and enter the interior of the IP based on ambient noise tomography at SW China and northern Vietnam (Qiao et al., 2018). High regional heat flow, shallow earthquakes, and low elastic thickness at the Shan-Thai Block also indicate the existence of a weak lower crust with low flexural rigidity and high temperature (Searle & Morley, 2011), which is further supported by isolated high Vp/Vs ratios from RF studies (e.g., Feng et al., 2021; Yu, Hung, et al., 2017). Dominant N-S fast orientations of crustal horizontal anisotropy were revealed from the SE Tibet to the Shan-Thai Block by a large-scale Rayleigh-wave anisotropic tomography for East Asia (Z. Huang et al., 2004), consistent with shearing directions expected from southward directed flow. In addition, mantle melts associated with the oblique Indo-Burma subduction (e.g., Charusiri et al., 1993; Searle et al., 2007; Speranza et al., 2019) may contribute to the development of the middle-lower-crustal LVZ beneath the Shan-Thai Block like what revealed beneath the Myanmar area where similar low-velocity anomalies were observed at middle- to lower-crustal depths (Wu et al., 2021). However, the absence of the expected LVZs underlying the Moho in our velocity model (Figure 8) may rule out the dominant role of the subduction effect. Therefore, our observations show that the eastern branch of the lower-crustal flow from the SE Tibet has extended into the IP

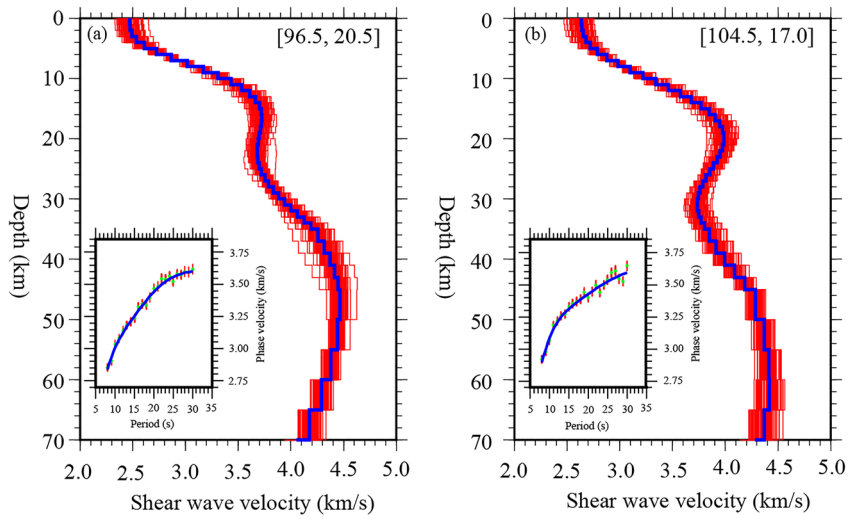

Figure 6. Examinations of random errors on the Vs inversion at two typical points with coordinates shown in the top right. The red lines in (a) and (b) are the inverted Vs models from the correspondingly 100 Rayleigh-wave dispersion curves (red dots) in the inset map generated by adding random deviations (in the range of −1% to +1%) of the observations (green dots). The blue solid lines indicate the final Vs model with the predicated dispersion curves (blue solid lines) shown in the insert map.

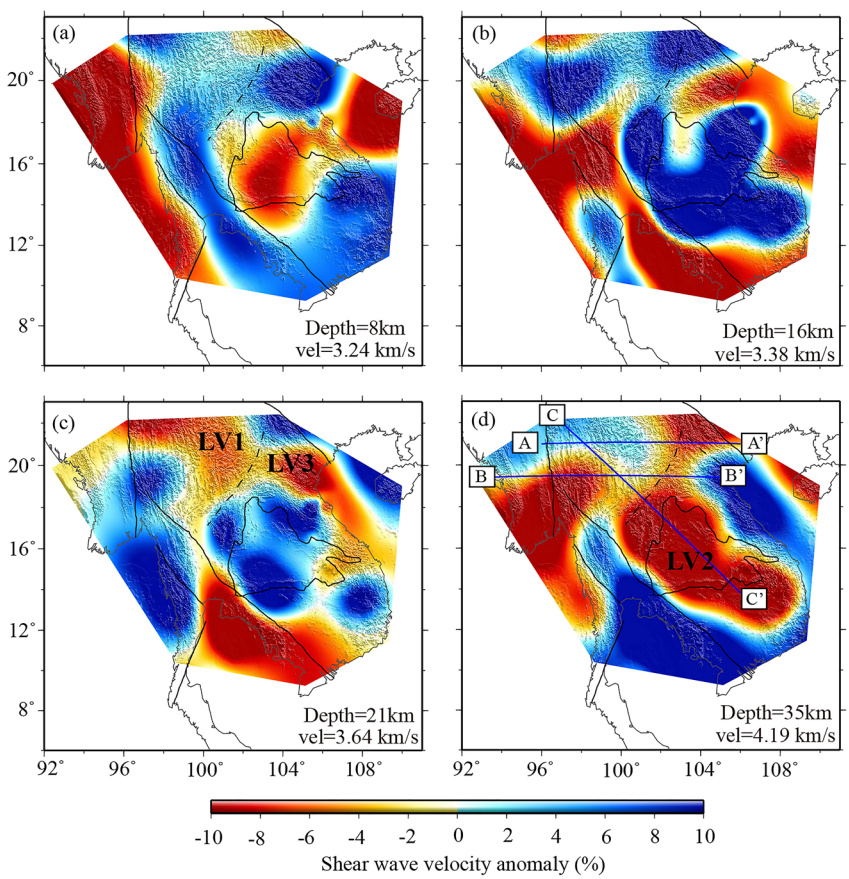

Figure 7. Contour maps of the resulting Vs anomalies at typical depths of 8 km (a), 16 km (b), 21 km (c), and 35 km (d). The background reference Vs is shown at the bottom right.

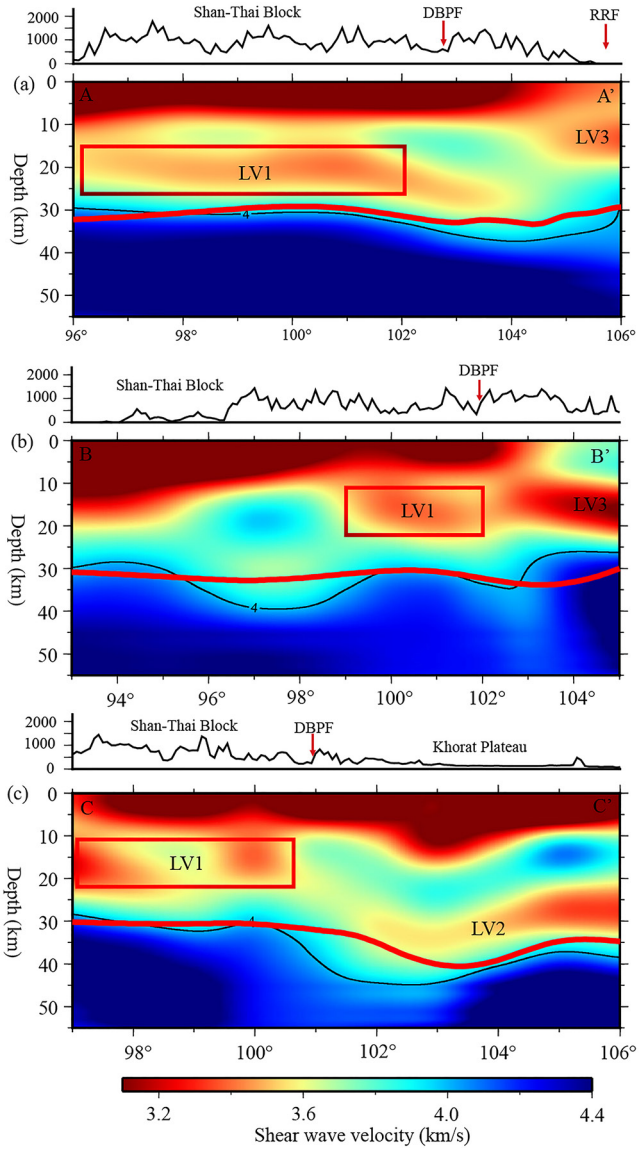

Figure 8. Vertical sections of the topography (top panel) and Vs structure (lower panel) along the three profiles in Figure 7d. The red rectangles highlight the low-velocity anomaly zones beneath the Shan-Thai Block. The red lines display the Moho depths combined from Nguyen et al. (2013), Noisagool et al. (2014), Yu, Hung, et al. (2017), and the CRUST 1.0 model (Laske et al., 2013).

and terminated at the DBPF (possibly blocked by the rigid Khorat Plateau), leading to the development of a mechanically weak crust as revealed by the intra-middle-lower-crustal LVZ beneath the Shan-Thai Block.

5.2. Crustal Modification Beneath the Khorat Plateau

The Khorat Plateau, acting as the core of the IP, has been considered as a rigid block without obvious crustal or lithospheric thinning during the southeastern extrusion of the IP since the Cenozoic (e.g., Takemoto et al., 2009; T. Yang et al., 2015; Yu, Hung, et al., 2017). The resulting low-velocity anomalies (LV2 in Figure 8) in the lower crust (depths of 25–35 km) indicate that the crustal structure beneath the Khorat Plateau may have been partially modified. A similar low-velocity anomaly is also revealed from the 3-D Vs model of the South China Sea and adjacent areas from joint inversion of ambient noise and earthquake surface wave dispersions though the resolution is not high (Chen et al., 2021). Basaltic rocks associated with intraplate volcanism dating at early Pleistocene have been reported in the interior of the Khorat Plateau and were further determined to include asthenospheric materials (Zhou & Mukasa, 1997). An asthenospheric source is also proposed to explain the Cenozoic volcanism of Southeast Asia (Fedorov & Koloskov, 2005). In contrast to what is observed beneath the Shan-Thai Block, the observed low-velocity anomaly in the lower crust of the Khorat Plateau seems to connect to a region of lower velocities in the mantle (Figure 8c around 50 km depth at 100°–103°E). A slab segment is revealed to exist in the mantle transition zone directly beneath the Khorat Plateau (Li & Van Der Hilst, 2010; Pesicek et al., 2008; Yu, Gao, et al., 2017; Yu et al., 2018). Dehydration melting and downwelling of this slab segment can trigger mantle upwelling, which supports the shallow volcanism (Yu, Gao, et al., 2017; Yu et al., 2018) and is consistent with the localized low-velocity anomaly in the top asthenosphere (150–230 km) beneath the Khorat Plateau (Chen et al., 2021; D. Zhao et al., 2021). However, the crust of the Khorat Plateau is characterized as possessing a generally felsic-to-intermediate composition based on observations from RF inversions (Noisagool et al., 2014; Yu, Hung, et al., 2017) and there is a lack of extensive volcanism in the interior (Figure 1). Thus, we propose that the crust of the Khorat Plateau has been partially modified from mantle-derived melts from an asthenospheric source. The absence of extensive volcanism at the Khorat Plateau is possibly due to the thick and rigid properties of its crust, which prevents substantial intrusions of mantle-derived melts.

5.3. Crustal Deformation Near the RRF

The RRF is a lithospheric scale strike-slip fault that represents boundary between the IP and the South China Block (H.-H. Huang et al., 2013; Legendre et al., 2015; X. Yang et al., 2021). The resulting low-velocity anomaly in the upper-middle crust is mostly revealed in the south-western flank of the RRF near the Song-Ma suture area (LV3 in Figures 7 and 8) and agrees well with those determined from recent Rayleigh-wave tomography of a regionally dense array in northern Vietnam (Legendre et al., 2015; Qiao et al., 2018; X. Yang et al., 2021). Such a low-velocity anomaly may be associated with an intense deformation from the strike-slip shear motions of the RRF, which is supported by the significant fault-parallel azimuthal anisotropy at the upper-middle crust (Legendre et al., 2015). Structural geological analysis along the RRF shear zone suggested that there is simple shearing within the brittle to ductile transition at mid-crustal levels, promoting the development of deformation structures, microstructures, and fabrics (J. Liu et al., 2012). High Vp/Vs ratios (Yu, Hung, et al., 2017) and the absence of extensive earthquakes may also indicate a ductile crust (L. Bai et al., 2010). Combined analyses of structural geology, metamorphic petrology,

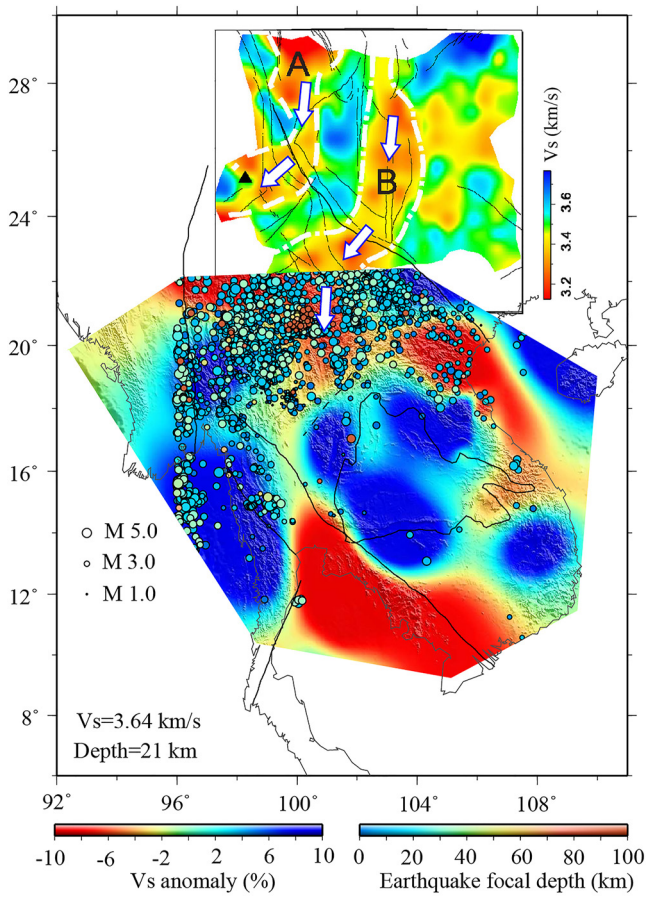

Figure 9. Joint display of the resulting Vs structure from this and previous studies at 21 km depth showing the crustal flow from SE Tibet. The inset represents results from Bao, Sun, et al. (2015) with A and B depicting the western and eastern branches of the crustal flow, respectively. The color dots are earthquakes occurring between 1970 and 2019 (downloaded from the International Seismological Centre, http://www.isc.ac.uk).

and $^{40}Ar/^{39}Ar$ thermochronology along the RRF deciphered prograde metamorphism associated with high temperature and crustal melting (Leloup et al., 1999, 2001). A low-velocity anomaly and thin lithosphere is imaged in the upper mantle at the western flank of the RRF (H.-H. Huang et al., 2013; Mi et al., 2021; Vu et al., 2021; T. Yang et al., 2015), which possibly indicates partial melting, which could lead to accumulation of mantle-derived melts in the overlying crust, where it could contribute to the observed low-velocity anomaly in the upper-middle crust. Coupled deformation between the lithosphere and asthenosphere is revealed from the shear-wave splitting analysis in northern Vietnam where the absolute plate motion partially works as an essential role (Yu et al., 2018). The petrogenesis of Cenozoic basalts in northern Vietnam also favors the model of decompression melting in the shallow upper mantle induced by mantle upwelling (Hoang & Flower, 1998; Hoang et al., 2013).

6. Conclusion

In this study, we have presented a 3-D shear-wave velocity model of the crust beneath the IP by conducting an ambient noise tomography based on data from a total of 38 stations and periods 8–30 s. The resulting velocity model resolves crust and uppermost mantle to a depth of 40–50 km for most of the areas (especially under the Khorat Plateau) with a lateral resolution of about 300 km. The model reveals a continuous middle-lower-crustal low-velocity anomaly in the Shan-Thai Block, which we interpret as evidence that lower-crustal flow from SE Tibet has extended into the Shan-Thai Block. A similar low-velocity anomaly is also revealed in the middle-lower crust of the Khorat Plateau, the core of the Indochina Block, and implies the presence of mantle-derived melts when combined with previous geochemical and geophysical results. Crustal deformation of the crust at the west flank of the RRF is inferred from the resulting low-velocity anomaly in the upper-middle crust and mostly induced by the strike-slip shearing with partially contributed from mantle-derived melts.

Data Availability Statement

We thank the Incorporated Research Institutions for Seismology (IRIS) Data Management Center (https://ds.iris.edu/ds/nodes/dmc) for archiving the dominant data used in this study and the Earthquake Research Institute of the University of Tokyo (http://ohpdmc.eri.u-tokyo.ac.jp/breq-fast-vietnet/) for sharing the data deployed in Vietnam. Data from another six temporary stations in Vietnam were collected by Tongji University. Cross-correlation waveforms are available as restricted data set at Zenodo (https://doi.org/10.5281/zenodo.5318617) upon request.

Acknowledgments
This study is supported by the National Natural Science Foundation of China (grant 42074052), the State Key Laboratory of Marine Geology, Tongji University (no. MG201902), and Shanghai Sheshan National Geophysical Observatory (grants 2020K04 and SSKP202103). Two anonymous reviewers provided insightful comments that greatly improved the paper.

References

Achache, J., Courtillot, V., & Besse, J. (1983). Paleomagnetic constraints on the late Cretaceous and Cenozoic tectonics of southeastern Asia. *Earth and Planetary Science Letters*, *63*, 123–136. https://doi.org/10.1016/0012-821X(83)90028-6

Bai, D., Unsworth, M. J., Meju, M. A., Ma, X., Teng, J., Kong, X., et al. (2010). Crustal deformation of the eastern Tibetan Plateau revealed by magnetotelluric imaging. *Nature Geoscience*, *3*(5), 358–362. https://doi.org/10.1038/ngeo830

Bai, L., Tian, X., & Ritsema, J. (2010). Crustal structure beneath the Indochina Peninsula from teleseismic receiver functions. *Geophysical Research Letters*, *37*, L24308. https://doi.org/10.1029/2010GL044874

Bao, X., Song, X., & Li, J. (2015). High-resolution lithospheric structure beneath Mainland China from ambient noise and earthquake surface-wave tomography. *Earth and Planetary Science Letters*, *417*, 132–141. https://doi.org/10.1016/j.epsl.2015.02.024

Bao, X., Sun, X., Xu, M., Eaton, D. W., Song, X., Wang, L., et al. (2015). Two crustal low-velocity channels beneath SE Tibet revealed by joint inversion of Rayleigh wave dispersion and receiver functions. *Earth and Planetary Science Letters*, *415*, 16–24. https://doi.org/10.1016/j.epsl.2015.01.020

Bensen, G. D., Ritzwoller, M. H., Barmin, M. P., Levshin, A. L., Lin, F., Moschetti, M. P., et al. (2007). Processing seismic ambient noise data to obtain reliable broad-band surface wave dispersion measurements. *Geophysical Journal International*, *169*(3), 1239–1260. https://doi.org/10.1111/j.1365-246X.2007.03374.x

Bird, P. (2003). An updated digital model of plate boundaries. *Geochemistry, Geophysics, Geosystems*, *4*(3), 1027. https://doi.org/10.1029/2001GC000252

Brocher, T. A. (2005). Empirical relations between elastic wavespeeds and density in the Earth's crust. *Bulletin of the Seismological Society of America*, *95*(6), 2081–2092. https://doi.org/10.1785/0120050077

Charusiri, P., Clark, A. H., Farrar, E., Archibald, D., & Charusiri, B. (1993). Granite belts in Thailand: Evidence from the $^{40}Ar/^{39}Ar$ geochronological and geological syntheses. *Journal of Southeast Asian Earth Sciences*, *8*, 127–136. https://doi.org/10.1016/0743-9547(93)90014-G

Charusiri, P., Daorerk, V., Archibald, D., Hisada, K., & Ampaiwan, T. (2002). Geotectonic evolution of Thailand: A new synthesis. *Journal of the Geological Society of Thailand*, *1*, 1–20.

Chen, H., Li, Z., Luo, Z., Ojo, A. O., Xie, J., Bao, F., et al. (2021). Crust and upper mantle structure of the South China Sea and adjacent areas from the joint inversion of ambient noise and earthquake surface wave dispersions. *Geochemistry, Geophysics, Geosystems*, *22*, e2020GC009356. https://doi.org/10.1029/2020GC009356

Chen, H., Zhu, L., Wang, Q., Zhang, P., & Yang, Y. (2014). S-wave velocity structure of the North China from inversion of Rayleigh wave phase velocity. *Journal of Asian Earth Sciences*, *88*, 178–191. https://doi.org/10.1016/j.jseaes.2014.03.006

Cheng, C., Chen, L., Yao, H., Jiang, M., & Wang, B. (2013). Distinct variations of crustal shear wave velocity structure and radial anisotropy beneath the North China Craton and tectonic implications. *Gondwana Research*, *23*(1), 25–38. https://doi.org/10.1016/j.gr.2012.02.014

Clark, M. K., & Royden, L. H. (2000). Topographic ooze: Building the eastern margin of Tibet by lower crustal flow. *Geology*, *28*(8), 703–706. https://doi.org/10.1130/0091-7613(2000)28<703:TOBTEM>2.0.CO;2

Fan, X., & Chen, Q. (2019). Seismic constraints on the magmatic system beneath the Changbaishan volcano: Insight into its origin and regional tectonics. *Journal of Geophysical Research: Solid Earth*, *124*, 2003–2024. https://doi.org/10.1029/2018JB016288

Fedorov, P. I., & Koloskov, A. V. (2005). Cenozoic volcanism of Southeast Asia. *Petrology*, *13*, 352–380.

Feng, M., Chen, L., Wang, X., Wei, S., & Wang, X. (2021). Crustal structure and its tectonic implications in Sundaland and adjacent areas: Constraints from tele-seismic receiver functions. *Chinese Journal of Geophysics-Chinese Edition*, *64*(12), 4364–4377. https://doi.org/10.6038/cjg2021O0356

Herrmann, R. B. (2013). Computer programs in seismology: An evolving tool for instruction and research. *Seismological Research Letters*, *84*(6), 1081–1088. https://doi.org/10.1785/0220110096

Hoang, N., & Flower, M. (1998). Petrogenesis of Cenozoic basalts from Vietnam: Implication for origins of a 'Diffuse Igneous Province'. *Journal of Petrology*, *39*(3), 369–395. https://doi.org/10.1093/petroj/39.3.369

Hoang, N., Flower, M. F. J., Chi, C. T., Xuan, P. T., Quy, H. V., & Son, T. T. (2013). Collision-induced basalt eruptions at Pleiku and Buôn Mê Thuộ, south-central Viet Nam. *Journal of Geodynamics*, *69*, 65–83. https://doi.org/10.1016/j.jog.2012.03.012

Hu, S., He, L., & Wang, J. (2000). Heat flow in the continental area of China: A new data set. *Earth and Planetary Science Letters*, *179*, 407–419. https://doi.org/10.1016/S0012-821X(00)00126-6

Huang, H., Yao, H., & Van der Hilst, R. D. (2010). Radial anisotropy in the crust of SE Tibet and SW China from ambient noise interferometry. *Geophysical Research Letters*, *37*, L21310. https://doi.org/10.1029/2010GL044981

Huang, H.-H., Xu, Z., Wu, Y.-M., Song, X., Huang, B.-S., & Nguyen, L. M. (2013). First local seismic tomography for Red River shear zone, northern Vietnam: Stepwise inversion employing crustal P and Pn waves. *Tectonophysics*, *584*, 230–239. https://doi.org/10.1016/j.tecto.2012.03.030

Huang, Z., Peng, Y., Luo, Y., Zheng, Y., & Su, W. (2004). Azimuthal anisotropy of Rayleigh waves in East Asia. *Geophysical Research Letters*, *31*, L15617. https://doi.org/10.1029/2004GL020399

Huchon, P., Lepichon, X., & Rangin, C. (1994). Indo-China Peninsula and the collision of India and Eurasia. *Geology*, *22*(1), 27–30. https://doi.org/10.1130/0091-7613(1994)022<0027:IPATCO>2.3.CO;2

Kennett, B. L. N., & Engdahl, E. R. (1991). Traveltimes for global earthquake location and phase identification. *Geophysical Journal International*, *105*, 429–465. https://doi.org/10.1111/j.1365-246X.1991.tb06724.x

Kennett, B. L. N., Engdahl, E. R., & Buland, R. (1995). Constraints on seismic velocities in the Earth from traveltimes. *Geophysical Journal International*, *122*(1), 108–124. https://doi.org/10.1111/j.1365-246x.1995.tb03540.x

Kong, F., Wu, J., Liu, K. H., & Gao, S. S. (2016). Crustal anisotropy and ductile flow beneath the eastern Tibetan Plateau and adjacent areas. *Earth and Planetary Science Letters*, *442*, 72–79. https://doi.org/10.1016/j.epsl.2016.03.003

Laske, G., Masters, G., Ma, Z., & Pasyanos, M. (2013). Update on CRUST1.0—A 1-degree global model of Earth's crust. In *Geophysical Research Abstracts* (Vol. 15, p. 2658). Vienna, Austria: EGU.

Legendre, C. P., Zhao, L., Huang, W.-G., & Huang, B.-S. (2015). Anisotropic Rayleigh-wave phase velocities beneath northern Vietnam. *Earth Planets and Space*, *67*(1), 28. https://doi.org/10.1186/s40623-015-0193-3

Leloup, P. H., Arnaud, N., Lacassin, R., Kienast, J. R., Harrison, T. M., Trong, T. T. P., et al. (2001). New constraints on the structure, thermochronology, and timing of the Ailao Shan–Red River shear zone, SE Asia. *Journal of Geophysical Research*, *106*(B4), 6683–6732. https://doi.org/10.1029/2000JB900322

Leloup, P. H., Lacassin, R., Tapponnier, P., Schärer, U., Zhong, D., Liu, X., et al. (1995). The Ailao Shan–Red River shear zone (Yunnan, China), tertiary transform boundary of Indochina. *Tectonophysics*, *251*, 3–84. https://doi.org/10.1016/0040-1951(95)00070-4

Leloup, P. H., Ricard, Y., Battaglia, J., & Lacassin, R. (1999). Shear heating in continental strike-slip shear zones: Model and field examples. *Geophysical Journal International*, *136*(1), 19–40. https://doi.org/10.1046/j.1365-246X.1999.00683.x

Lepvrier, C., Maluski, H., Van Tich, V., Leyreloup, A., Truong Thi, P., & Van Vuong, N. (2004). The Early Triassic Indosinian orogeny in Vietnam (Truong Son Belt and Kontum Massif); implications for the geodynamic evolution of Indochina. *Tectonophysics*, *393*, 87–118. https://doi.org/10.1016/j.tecto.2004.07.030

Levshin, A. L., & Ritzwoller, M. H. (2001). Automated detection, extraction, and measurement of regional surface waves. *Pure and Applied Geophysics*, *158*(8), 1531–1545. https://doi.org/10.1007/PL00001233

Li, C., & Van Der Hilst, R. D. (2010). Structure of the upper mantle and transition zone beneath Southeast Asia from traveltime tomography. *Journal of Geophysical Research*, *115*, B07308. https://doi.org/10.1029/2009JB006882

Lin, F.-C., Moschetti, M. P., & Ritzwoller, M. H. (2008). Surface wave tomography of the western United States from ambient seismic noise: Rayleigh and Love wave phase velocity maps. *Geophysical Journal International*, *173*(1), 281–298. https://doi.org/10.1111/j.1365-246x.2008.03720.x

Liu, C., Yao, H., Yang, H.-Y., Shen, W., Fang, H., Hu, S., & Qiao, L. (2019). Direct inversion for three-dimensional shear wave speed azimuthal anisotropy based on surface wave ray tracing: Methodology and application to Yunnan, southwest China. *Journal of Geophysical Research: Solid Earth*, *124*, 11394–11413. https://doi.org/10.1029/2018JB016920

Liu, J., Tang, Y., Tran, M.-D., Cao, S., Zhao, L., Zhang, Z., et al. (2012). The nature of the Ailao Shan–Red River (ASRR) shear zone: Constraints from structural, microstructural and fabric analyses of metamorphic rocks from the Diancang Shan, Ailao Shan and Day Nui Con Voi massifs. *Journal of Asian Earth Sciences*, *47*, 231–251. https://doi.org/10.1016/j.jseaes.2011.10.020

Mi, Q., Lei, J., Du, M., He, J., Lu, H., Sun, C., et al. (2021). Pn anisotropic tomography and mantle dynamics underneath the South China Sea and surrounding areas. *Journal of Asian Earth Sciences*, *214*, 104796. https://doi.org/10.1016/j.jseaes.2021.104796

Montagner, J.-P., & Nataf, H.-C. (1986). A simple method for inverting the azimuthal anisotropy of surface waves. *Journal of Geophysical Research*, *91*(B1), 511–520. https://doi.org/10.1029/JB091iB01p00511

Morley, C. K. (2002). A tectonic model for the Tertiary evolution of strike–slip faults and rift basins in SE Asia. *Tectonophysics*, *347*, 189–215. https://doi.org/10.1016/S0040-1951(02)00061-6

Nguyen, V.-D., Huang, B.-S., Le, T.-S., Dinh, V.-T., Zhu, L., & Wen, K.-L. (2013). Constraints on the crustal structure of northern Vietnam based on analysis of teleseismic converted waves. *Tectonophysics*, *601*, 87–97. https://doi.org/10.1016/j.tecto.2013.04.031

Noisagool, S., Boonchaisuk, S., Pornsopin, P., & Siripunvaraporn, W. (2014). Thailand's crustal properties from tele-seismic receiver function studies. *Tectonophysics*, *632*, 64–75. https://doi.org/10.1016/j.tecto.2014.06.014

Pesicek, J. D., Thurber, C. H., Widiyantoro, S., Engdahl, E. R., & DeShon, H. R. (2008). Complex slab subduction beneath northern Sumatra. *Geophysical Research Letters*, *35*, L20303. https://doi.org/10.1029/2008GL035262

Qiao, L., Yao, H., Lai, Y.-C., Huang, B.-S., & Zhang, P. (2018). Crustal structure of southwest China and northern Vietnam from ambient noise tomography: Implication for the large-scale material transport model in SE Tibet. *Tectonics*, *37*, 1492–1506. https://doi.org/10.1029/2018TC004957

Racey, A. (2009). Mesozoic red bed sequences from SE Asia and the significance of the Khorat Group of NE Thailand. *Geological Society, London, Special Publications*, *315*, 41–67. https://doi.org/10.1144/SP315.5

Royden, L. H., Burchfiel, B. C., & Van Der Hilst, R. D. (2008). The geological evolution of the Tibetan Plateau. *Science*, *321*, 1054–1058. https://doi.org/10.1126/science.1155371

Sato, K., Liu, Y., Wang, Y., Yokoyama, M., Yoshioka, S. Y., Yang, Z., & Otofuji, Y.-I. (2007). Paleomagnetic study of Cretaceous rocks from Pu'er, western Yunnan, China: Evidence of internal deformation of the Indochina block. *Earth and Planetary Science Letters*, *258*, 1–15. https://doi.org/10.1016/j.epsl.2007.02.043

Searle, M. P., & Morley, C. K. (2011). Tectonic and thermal evolution of Thailand in the regional context of SE Asia. In *The geology of Thailand* (pp. 539–571). https://doi.org/10.1144/GOTH.20

Searle, M. P., Noble, S. R., Cottle, J. M., Waters, D. J., Mitchell, A. H. G., Hlaing, T., & Horstwood, M. S. A. (2007). Tectonic evolution of the Mogok metamorphic belt, Burma (Myanmar) constrained by U–Th–Pb dating of metamorphic and magmatic rocks. *Tectonics*, *26*, TC3014. https://doi.org/10.1029/2006TC002083

Speranza, F., Pellegrino, A. G., Zhang, B., Maniscalco, R., Chen, S., & Hernandez-Moreno, C. (2019). Paleomagnetic evidence for 25–15 Ma crust fragmentation of north Indochina (23–26°N): Consequence of collision with greater India NE corner? *Geochemistry, Geophysics, Geosystems*, *20*, 5425–5448. https://doi.org/10.1029/2019GC008308

Sun, X., Bao, X., Xu, M., Eaton, D. W., Song, X., Wang, L., et al. (2014). Crustal structure beneath SE Tibet from joint analysis of receiver functions and Rayleigh wave dispersion. *Geophysical Research Letters*, *41*, 1479–1484. https://doi.org/10.1002/2014GL059269

Takemoto, K., Sato, S., Chanthavichith, K., Inthavong, T., Inokuchi, H., Fujihara, M., et al. (2009). Tectonic deformation of the Indochina Peninsula recorded in the Mesozoic palaeomagnetic results. *Geophysical Journal International*, *179*, 97–111. https://doi.org/10.1111/j.1365-246X.2009.04274.x

Tapponnier, P., Peltzer, G., & Armijo, R. (1986). On the mechanics of the collision between India and Asia. *Geological Society, London, Special Publications*, *19*(1), 113–157. https://doi.org/10.1144/GSL.SP.1986.019.01.07

Tapponnier, P., Peltzer, G., Dain, A. Y., Armijo, R., & Cobbold, P. R. (1982). Propagating extrusion tectonics in Asia: New insights from simple experiments with plasticine. *Geology*, *10* (12), 611–616. https://doi.org/10.1130/0091-7613(1982)10<611:PETIAN>2.0.CO;2

Tarantola, A., & Valette, B. (1982). Generalized nonlinear inverse problems solved using the least squares criterion. *Reviews of Geophysics*, *20*(2), 219–232. https://doi.org/10.1029/RG020i002p00219

Vu, D. T., Bonvalot, S., Bruinsma, S., & Bui, L. K. (2021). A local lithospheric structure model for Vietnam derived from a high-resolution gravimetric geoid. *Earth Planets and Space*, *73*, 92. https://doi.org/10.1186/s40623-021-01415-2

Wei, Z., Chu, R., Chen, L., & Wu, S. (2020). Crustal structure in the middle-southern segments of the Tanlu Fault Zone and adjacent regions constrained by multifrequency receiver function and surface wave data. *Physics of the Earth and Planetary Interiors*, *301*, 106470. https://doi.org/10.1016/j.pepi.2020.106470

Wu, S., Yao, J., Wei, S., Hubbard, J., Wang, Y., Htwe, Y. M. M., et al. (2021). New insights into the structural heterogeneity and geodynamics of the Indo-Burma subduction zone from ambient noise tomography. *Earth and Planetary Science Letters*, *562*, 116856. https://doi.org/10.1016/j.epsl.2021.116856

Yang, T., Liu, F., Harmon, N., Le, K. P., Gu, S., & Xue, M. (2015). Lithospheric structure beneath Indochina block from Rayleigh wave phase velocity tomography. *Geophysical Journal International*, *200*(3), 1582–1595. https://doi.org/10.1093/gji/ggu488

Yang, X., Yao, H., & Huang, B.-S. (2021). Crustal footprint of mantle upwelling and plate amalgamation revealed by ambient noise tomography in northern Vietnam and the northern South China Sea. *Journal of Geophysical Research: Solid Earth*, *126*, e2020JB020593. https://doi.org/10.1029/2020JB020593

Yang, Y., Forsyth, D. W., & Weeraratne, D. S. (2007). Seismic attenuation near the East Pacific Rise and the origin of the low-velocity zone. *Earth and Planetary Science Letters*, *258*, 260–268. https://doi.org/10.1016/j.epsl.2007.03.040

Yao, H., Van Der Hilst, R. D., & de Hoop, M. V. (2006). Surface-wave array tomography in SE Tibet from ambient seismic noise and two-station analysis—I. Phase velocity maps. *Geophysical Journal International*, *166*, 732–744. https://doi.org/10.1111/j.1365-246X.2006.03028.x

Yao, H., Xu, G., Zhu, L., & Xiao, X. (2005). Mantle structure from inter-station Rayleigh wave dispersion and its tectonic implication in western China and neighboring regions. *Physics of the Earth and Planetary Interiors*, *148*(1), 39–54. https://doi.org/10.1016/j.pepi.2004.08.006

Yu, Y., Gao, S. S., Liu, K. H., Yang, T., Xue, M., & Le, K. P. (2017). Mantle transition zone discontinuities beneath the Indochina Peninsula: Implications for slab subduction and mantle upwelling. *Geophysical Research Letters*, *44*, 7159–7167. https://doi.org/10.1002/2017GL073528

Yu, Y., Gao, S. S., Liu, K. H., Yang, T., Xue, M., Le, K. P., & Gao, J. (2018). Characteristics of the mantle flow system beneath the Indochina Peninsula revealed by teleseismic shear wave splitting analysis. *Geochemistry, Geophysics, Geosystems*, *19*, 1519–1532. https://doi.org/10.1029/2018GC007474

Yu, Y., Hung, T. D., Yang, T., Xue, M., Liu, K. H., & Gao, S. S. (2017). Lateral variations of crustal structure beneath the Indochina Peninsula. *Tectonophysics*, *712–713*, 193–199. https://doi.org/10.1016/j.tecto.2017.05.023

Zhao, D., Toyokuni, G., & Kurata, K. (2021). Deep mantle structure and origin of Cenozoic intraplate volcanoes in Indochina, Hainan and South China Sea. *Geophysical Journal International*, *225*, 572–588. https://doi.org/10.1093/gji/ggaa605

Zhao, J., Li, Z., Lin, J., Hao, T., Bao, F., Xie, J., et al. (2019). Ambient noise tomography and deep structure in the crust and mantle of the South China Sea. *Chinese Journal of Geophysics*, *62*(6), 2070–2087. (in Chinese). https://doi.org/10.6038/cjg2019M0138

Zhao, L., Xie, X., He, J., Tian, X., & Yao, Z. (2013). Crustal flow pattern beneath the Tibetan Plateau constrained by regional Lg-wave Q tomography. *Earth and Planetary Science Letters*, *383*, 113–122. https://doi.org/10.1016/j.epsl.2013.09.038

Zhou, P., & Mukasa, S. B. (1997). Nd–Sr–Pb isotopic, and major- and trace-element geochemistry of Cenozoic lavas from the Khorat Plateau, Thailand: Sources and petrogenesis. *Chemical Geology*, *137*(3), 175–193. https://doi.org/10.1016/S0009-2541(96)00162-3